

Emerging Long-Range Order from a Freeform Disordered Metasurface

Mingfeng Xu, Qiong He, Mingbo Pu,* Fei Zhang, Ling Li, Di Sang, Yinghui Guo, Renyan Zhang, Xiong Li, Xiaoliang Ma, and Xiangang Luo*

Recently, disordered metasurfaces have attracted considerable interest due to their potential applications in imaging, holography, and wavefront shaping. However, how to emerge long-range ordered phase distribution in disordered metasurfaces remains an outstanding problem. Here, a general framework is proposed to generate a spatially homogeneous in-plane phase distribution from a disordered metasurface, by engineering disorder parameters together with topology optimization. As a proof-of-concept demonstration, an all-dielectric disordered supercell metasurface with relatively homogeneous in-plane phase fluctuation is designed by disorder parameter engineering, manifesting as polarization conversion-dependent random scattering or unidirectional transmission. Then, a topology optimization approach is utilized to overcome the lattice coupling effect and to further improve the homogeneity of complex electric field fluctuation. In comparison with the initial supercell metasurface, both the phase fluctuation range and the relative efficiency of the topology-optimized freeform metasurface are significantly improved, leading to a long-range ordered electric field distribution. Moreover, three experimental realizations are performed, all of which agree well with the theoretical results. This methodology may inspire more exotic optical phenomena and find more promising applications in disordered metasurfaces and disordered optics.

1. Introduction

Owing to the uncontrollable optical random scattering, irregular, or disordered structures have been considered as an unfavorable factor in the design and fabrication of traditional optical devices.^[1] For example, photonic crystal is a typical optical device consisting of ordered period structures, wherein the

existence of defect or disorder will inevitably result in the destruction of intrinsic photonic bandgaps, thus impairing the practical performance of desired design for wave propagation.^[2] By contrary, recent developments in micro- and nanophotonics have demonstrated that disorder structure with spatially inhomogeneous material, including random or chaotic structures, could be well utilized as another degree of freedom to yield various new optical phenomena.^[3–5] Particularly, a variety of nonconventional optical functionalities have been proposed in diverse areas of optical applications, ranging from optical Anderson localization in deep sub-wavelength photonic structures,^[6] broadband momentum transformation and spatiotemporal instability suppression in a chaotic optical microcavity,^[7,8] and optical transition in the disordered plasmonic system^[9,10] to perfect focusing in disordered media.^[11,12]

Consisting of arrays of artificial nanostructures (or meta-atoms), metasurface can arbitrarily manipulate the amplitude, phase, and polarization of the incident light field at subwavelength scale^[13–15] and therefore has been widely applied to planar imaging,^[16–19] meta-holograms,^[20–22] quantum optics,^[23–26] and complex beam generators.^[27–31] Most recently, disorder engineering has been introduced into metasurface by randomly manipulating the spatially inhomogeneous phase retardation of meta-atoms,

M. Xu, Q. He, M. Pu, F. Zhang, D. Sang, Y. Guo, R. Zhang, X. Li, X. Ma, X. Luo

State Key Laboratory of Optical Technologies on Nano-Fabrication and Micro-Engineering

Institute of Optics and Electronics

Chinese Academy of Sciences

Chengdu 610209, China

E-mail: pmb@ioe.ac.cn; lxx@ioe.ac.cn

M. Xu, D. Sang, R. Zhang

Division of Frontier Science and Technology

Institute of Optics and Electronics

Chinese Academy of Sciences

Chengdu 610209, China

M. Pu, Y. Guo, X. Li, X. Ma, X. Luo

School of Optoelectronics

University of Chinese Academy of Sciences

Beijing 100049, China

L. Li

Tianfu Xinglong Lake Laboratory


Chengdu 610299, China

D. Sang

College of Electronic Science and Technology

National University of Defense Technology

Changsha 410072, China

 The ORCID identification number(s) for the author(s) of this article can be found under <https://doi.org/10.1002/adma.202108709>.

DOI: 10.1002/adma.202108709

leading to disordered phase metasurface that serves as a compact and versatile platform for emerging intriguing functionalities.^[32–40] For example, completely disordering orientation-dependent geometric phase enables the emergence of random Rashba effect,^[33] while engineering the disordered guided mode propagation phase offers a unique capability for wavefront shaping with a large optical memory effect range.^[34] However, previous works mainly focused on the disorder functionality, while the opposite functionality—order in a disordered metasurface—is seriously neglected. In fact, the order that existed in disorder is an important concept and has been widely used in various disordered structures.^[41–43] Unfortunately, how to emerge long-range order in a disordered metasurface has been elusive.

Here, we propose a general framework for efficient design of long-range-ordered in-plane phase distribution, by engineering disorder parameters together with topology optimization in a supercell metasurface. Specifically, it is shown that spatially homogeneous in-plane phase distribution could be obtained in a disordered metasurface where both the propagation phase and geometric phase are randomly distributed. As a proof-of-concept demonstration, an all-dielectric disordered supercell metasurface is designed based on disordered parameter engineering, offering a relatively homogeneous phase fluctuation. Depending on different polarization conversions, the metasurface manifests as random scattering or unidirectional transmission. Moreover, a freeform disordered metasurface is further proposed by using adjoint-based topology optimization, which enables us to suppress both in-plane phase and in-plane amplitude fluctuations simultaneously. Notably, to the best of our knowledge, it is the first application of topology optimization in a disordered metasurface. As a result, the topology-optimized phase fluctuation range is improved about four times than that of the initial disordered supercell metasurface, while the relative efficiency of transmitted circularly polarized light is improved by about 39%. Furthermore, the theoretical results are well demonstrated by three different experiments. Our general framework could be simply extended to other types of phase retardation mechanisms, opening an exciting avenue to inspire more exotic optical phenomena in disordered metasurfaces and disordered optics.

2. Results

2.1. Principle of Disorder Parameter Engineering

Without loss of generality, we consider a disordered metasurface that includes both disordered propagation phase and disordered geometric phase. As shown in **Figure 1a–c**, the disordered phase metasurface is designed as a supercell structure to realize random-in-plane phase distribution, wherein each supercell contains several meta-atoms. **Figure 1a,d** present the supercell metasurface with disordered propagation phase, where both width $w(x,y)$ and length $l(x,y)$ of every nanorod in meta-atom are randomly varied. Such random-in-plane propagation phase could be defined as $\Xi_p(x,y) = \varepsilon_p(x,y) \cdot 2\pi$, where $\varepsilon_p(x,y) \in [0,1]$ is a disorder parameter of propagation phase. It obeys uniform distribution and is determined by the random

$w(x,y)$ and $l(x,y)$. Similarly, the geometric phase-disordered metasurface is presented in **Figure 1b,e**, where the disordered phase retardation distribution for transmitted cross-polarization light depends on the spatial-randomly variant orientation $\theta(x,y)$ of nanorods. Particularly, the random-in-plane geometric phase can be written as $\Xi_g(x,y) = \pm 2\theta(x,y) = \pm \varepsilon_g(x,y) \cdot 2\pi$, where $\varepsilon_g(x,y) \in [0,1]$ denotes uniformly distributed disorder parameter of geometric phase and the sign \pm depends on the chirality of incident light.

As indicated in **Figure 1c,f**, when all the structural parameters $w(x,y)$, $l(x,y)$, and $\theta(x,y)$ of every nanorod are randomly varied, the transmitted cross-polarization light through such disordered metasurface acquires both random propagation phase retardation and random geometric phase retardation. Therefore, total random-in-plane phase accumulation for cross-polarization and co-polarization conversions in the disordered metasurface is governed by

$$\begin{cases} \Xi_{|R\rangle \rightarrow |R\rangle} = \Xi_{|L\rangle \rightarrow |L\rangle} = 2\pi \cdot \varepsilon_p(x,y) \\ \Xi_{|R\rangle \rightarrow |L\rangle} = 2\pi \cdot [\varepsilon_p(x,y) - \varepsilon_g(x,y)] \\ \Xi_{|L\rangle \rightarrow |R\rangle} = 2\pi \cdot [\varepsilon_p(x,y) + \varepsilon_g(x,y)] \end{cases} \quad (1)$$

where $|L\rangle$ and $|R\rangle$ denote left- and right-handed circular polarizations (LCP and RCP), respectively.

Equation (1) reveals that, similar to the composite-phase engineering approach in ordered metasurface, it is possible to emerge long-range ordered phase distribution in such disordered metasurface by elaborately engineering the disorder parameters $\varepsilon_p(x,y)$ and $\varepsilon_g(x,y)$. For instance, homogeneous in-plane phase distribution, that is, long-range order, could be obtained when $\varepsilon_p(x,y) = -\varepsilon_g(x,y)$, as shown in **Figure 1i**. In contrast, when only one disorder parameter affects (**Figure 1g**) or two disorder parameters are mismatched (**Figure 1h**), the in-plane phase accumulation is still spatial-randomly distributed. Note that when i) the disorder parameters $\varepsilon_p(x,y)$ and $\varepsilon_g(x,y)$ are constant, that is, the structural parameters $w(x,y)$, $l(x,y)$, and $\theta(x,y)$ are not randomly varied, ii) the supercell becomes trivial, that is, it only contains one meta-atom, the Equation (1) degenerates into Equation (S1) in Supporting Information (see Section S1, Supporting Information for details). Therefore, disorder parameter engineering is a more general formalism of composite-phase manipulation that is prevalently proposed in ordered metasurfaces.^[44–48]

2.2. Disordered Supercell Metasurface

As an example, we utilize the abovementioned disorder parameter engineering to emerge long-range order from the disordered metasurface shown in **Figure 1c**. **Figure 2a** presents the designed all-dielectric disordered metasurface, including the corresponding geometrical structure of meta-atoms. In particular, the disordered supercell metasurface contains 121 of meta-atoms, including 11 of sub-periods in each direction. The period of meta-atoms and the height of nanorods keep constant, that is, $p_x = p_y = 3.1 \mu\text{m}$ and $h = 8 \mu\text{m}$ for each meta-atom. Meanwhile, the other three geometrical parameters (i.e., width w , length l , and orientation θ) are randomly changed for dif-

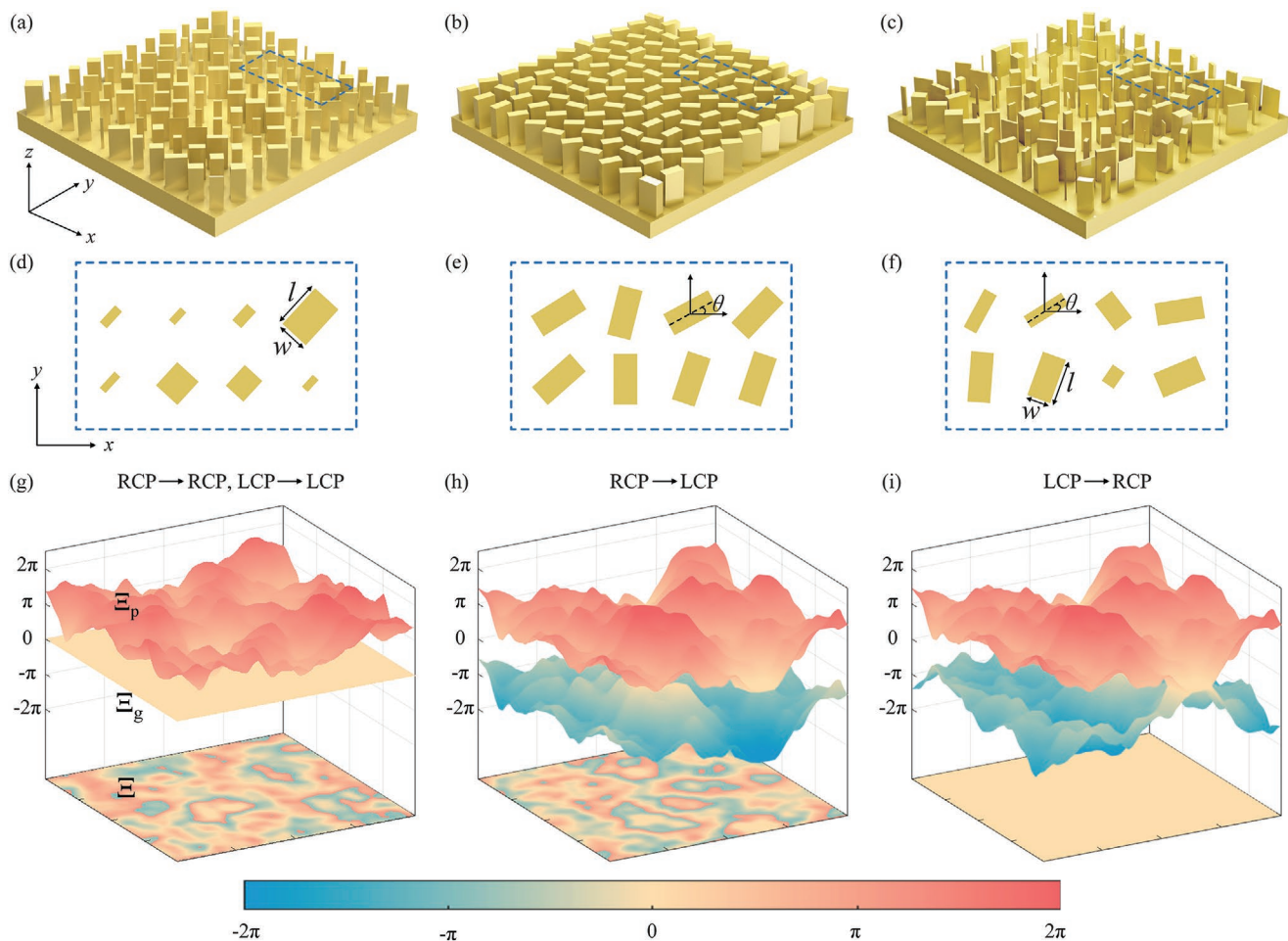


Figure 1. Concept of disorder parameter engineering in the disordered metasurface. a–c) Disordered supercell metasurface exhibiting disordered propagation phase (a), disordered geometric phase (b), and disordered composite-phase (c). d–f) Meta-atoms arrangement of the disordered metasurface, corresponding to the blue dashed frame in (a–c), respectively. In (d), width w and length l of nanorods are random; In (e), orientation θ is random; In (f), all the three structural parameters are randomly varied. g–i) Disordered phase distribution of different circularly polarized light transmitted from disordered composite-phase metasurface shown in (c), for co-polarization conversion (g) and cross-polarization conversion (h,i). Ξ_p , Ξ_g , and Ξ indicate disordered propagation phase, disordered geometric phase, and disordered composite-phase, respectively. For clarity, the range of Ξ_p , Ξ_g , and Ξ are set to $[0, 2\pi]$, $[-2\pi, 0]$, and $[-\pi, \pi]$, respectively.

ferent meta-atoms. Based on such supercell structure, we first generate the disordered parameter ϵ_g (i.e., random geometric phase distribution) by randomly varying the orientation θ of meta-atoms. Once the ϵ_g is confirmed, we then scan the specific parameter space of (w, l) from the structure parameter library for every nanorod, making ϵ_p a valid match with ϵ_g . It is worth mentioning that the supercell period of $34.1 \mu\text{m}$ is selected based on the balance of disorder functionality and computational resource. The amplitude and phase of transmitted light for cross-polarization conversion as functions of w and l are presented in Figure 2b, where the library range is $w \in [0.1p_x, 0.9p_x] = [0.31 \mu\text{m}, 2.79 \mu\text{m}]$ and $l \in [0.1p_y, 0.9p_y] = [0.31 \mu\text{m}, 2.79 \mu\text{m}]$. It shows that the propagation phase range of $[0, 2\pi]$ could be covered and relatively high amplitude could be simultaneously achieved by properly selecting w and l .

Figure 2c,d present the in-plane amplitude and phase distribution of polarized light transmitted from the disordered supercell metasurface under different co-polarization and cross-polariza-

tion conversions. For the co-polarization conversions ($|R\rangle \rightarrow |R\rangle$ and $|L\rangle \rightarrow |L\rangle$) where only disorder parameter ϵ_p affects, as shown in the first two columns in Figure 2c,d, the transmitted circularly polarized light has spatially random in-plane amplitude and phase distribution. A similar situation appears when the two disorder parameters ϵ_p and ϵ_g are mismatched ($|R\rangle \rightarrow |L\rangle$), as presented in the third column of Figure 2c,d. In contrast, the last column of Figure 2c,d indicate that, when ϵ_p and ϵ_g are matched exactly ($|L\rangle \rightarrow |R\rangle$), spatially homogeneous amplitude and phase distribution emerge in the disordered supercell metasurface. Moreover, simulated transmitted electric field distribution in xoz plane confirms that the matched cross-polarization conversion ($|L\rangle \rightarrow |R\rangle$) possesses a uniform wavefront, leading to directional transmission along the normal direction (see Figure S1, Supporting Information for details). On the contrary, for other mismatched cross-polarization conversions, the transmitted electric field has heterogeneous wavefronts, thus manifesting as unidirectional, random scattering.

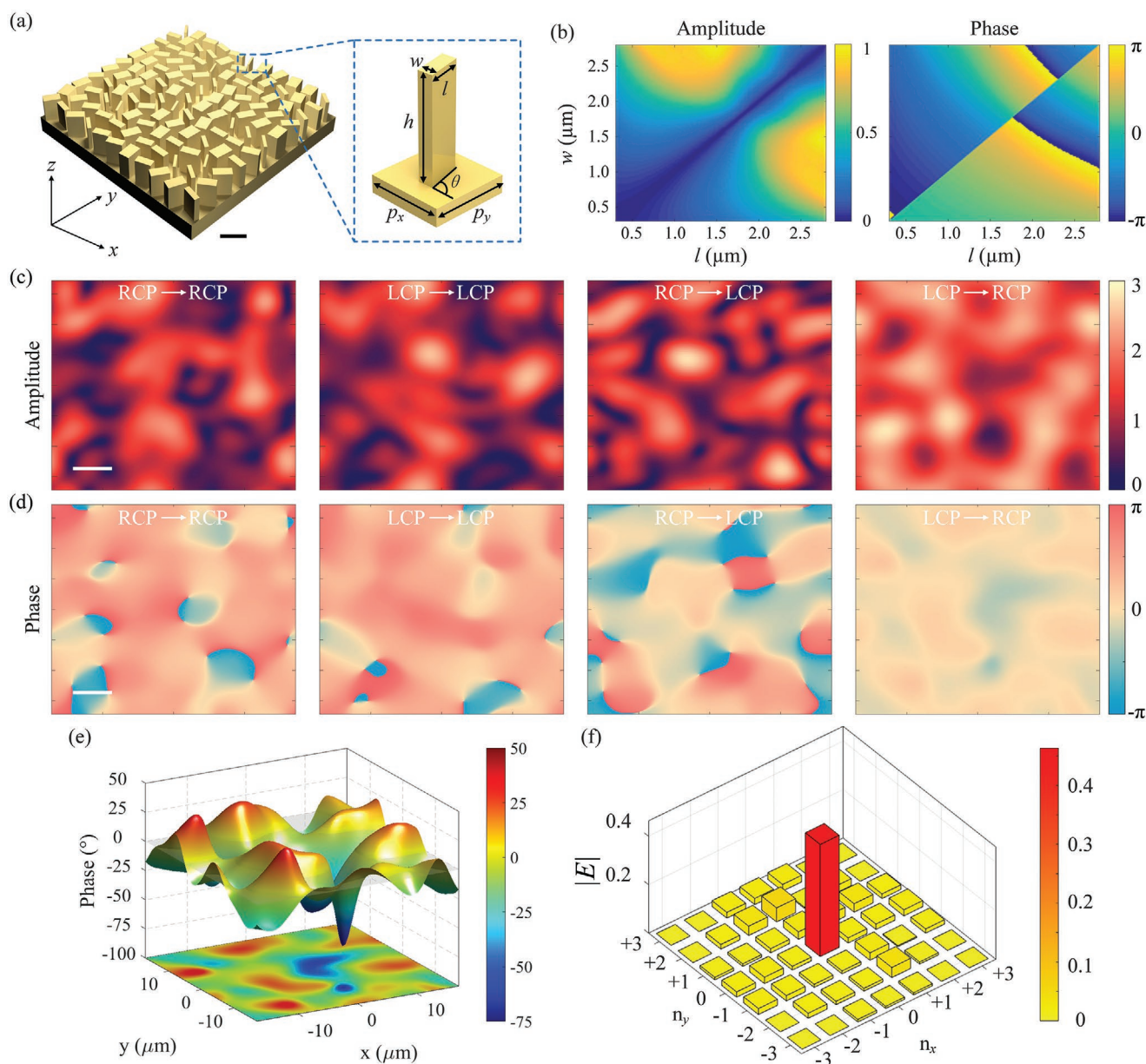


Figure 2. Disordered supercell metasurface. a) Schematic of disordered supercell metasurface. The inset shows the geometrical parameters of meta-atom, where $p_x = p_y = 3.1 \mu\text{m}$ and $h = 8 \mu\text{m}$. The width w , length l , and orientation θ are randomly varied for different meta-atoms. Scale bar: $5 \mu\text{m}$. b) Parameter library of transmitted amplitude and phase as functions of w and l for solitary meta-atom. c,d) In-plane amplitude and phase distribution of transmitted light for different polarization conversions. Scale bar: $5 \mu\text{m}$. e) 3D distribution of phase fluctuation of transmitted light for $|L\rangle \rightarrow |R\rangle$ conversion. The gray plane indicates the zero line of phase fluctuation. The projection of 3D distribution in the xoy plane corresponds to the phase distribution in the fourth column of (d). f) Simulated amplitude distributions in different diffraction orders for $|L\rangle \rightarrow |R\rangle$ conversion.

To characterize the spatial homogeneity of in-plane phase distribution, the 3D distribution of phase fluctuation for $|L\rangle \rightarrow |R\rangle$ conversion is further presented in Figure 2e. It shows that, although the disordered parameters are optimized by using the parameter scanning approach, the in-plane phase distribution still has an apparent fluctuation between $[-65^\circ, 35^\circ]$, leading to a fluctuation range of about 100° . Moreover, the corresponding probability distribution of phase in meta-atoms shows that there still has plenty of room for the improvement of phase homogeneity (see Figure S2, Supporting Informa-

tion for details). Furthermore, Figure 2f presents the simulated amplitude distributions in different diffraction orders for matched cross-polarization conversion ($|L\rangle \rightarrow |R\rangle$), where the (0,0) diffraction order dominates the transmitted light energy (see Figure S3, Supporting Information for other polarization conversions). In fact, the absolute efficiency of transmitted RCP light in (0,0) diffraction order and other higher diffraction orders are 21.44% and 2.10%, respectively (see Figure S4, Supporting Information for details). Therefore, the (0,0) diffraction order energy ratio of RCP light defined as $\eta = I_{(0,0)}/I$, where

$I(0,0)$ and I respectively denote the light intensity in the (0,0) diffraction order and the total intensity of transmitted RCP light, is about 91.08%. Furthermore, the simulation results of diffraction intensity show that when the LCP light is incident at the disordered metasurface, the relative efficiency of transmitted RCP light is calculated as 69.14%.

2.3. Freeform Disordered Metasurface

As shown in Figure 2, there still has distinct fluctuations in the in-plane amplitude and phase distribution, although the structure parameters have been elaborately optimized. In essence, the unavoidable resonance coupling between adjoint meta-atoms in the discrete subwavelength structure is the main cause of such undesirable fluctuations. In comparison with discrete structure, however, the continuous structure could effectively suppress the resonance coupling and has the potential ability to eliminate the undesirable in-plane electric field fluctuations.^[49] Therefore, we further demonstrate a quasi-continuous freeform disordered metasurface by using the topology optimization approach (see Experimental Section for details).

The evolutions of the figure of merit (FoM) in the topology optimization process is presented in Figure 3a. It shows that the FoM of final freeform metasurface presented in Figure 3b has been improved more than threefold compared with the initial metasurface. Figure 3c,d indicate the corresponding in-plane amplitude and phase distribution of transmitted polarized light under different co-polarization and cross-polarization conversions. In comparison with Figure 2c,d, Figure 3c,d clearly reveal that, attributing to the efficient suppression of complex electric field fluctuations during the topology optimization process, the spatial homogeneity of in-plane amplitude and phase distribution for $|L\rangle \rightarrow |R\rangle$ conversion are both dramatically improved. More importantly, Figure 3e shows that the in-plane phase fluctuation for $|L\rangle \rightarrow |R\rangle$ conversion is greatly condensed to $[-17^\circ, 10^\circ]$. Therefore, the phase fluctuation range (27°) is reduced about four times than that of the initial supercell metasurface shown in Figure 2e. Moreover, the phase probability distribution presented in Figure 3f also shows the superior spatial homogeneity of the topology-optimized freeform disorder metasurface.

Figure 4a,b present the simulated electric field distribution of transmitted cross-polarization light. On the one hand, in comparison with the fragmented wavefront shown in Figure 4a for $|R\rangle \rightarrow |L\rangle$ conversion, Figure 4b exhibits a more complete and ordered wavefront for $|L\rangle \rightarrow |R\rangle$ conversion. The other mismatched co-polarization conversions also exhibit the random wavefront (see Figure S5, Supporting Information for details). On the other hand, Figure 4b also shows that the topology-optimized freeform metasurface has a more smooth wavefront distribution in comparison with that of the initial metasurface (see Figure S1d, Supporting Information). Therefore, the freeform metasurface possesses a better functionality of directional transmission for $|L\rangle \rightarrow |R\rangle$ conversion, which is further demonstrated in Figure 4d. It shows that the vast majority of transmitted light energy concentrates in the (0,0) diffraction order. In particular, the corresponding absolute efficiency of transmitted

RCP light in the (0,0) diffraction order is 38.33% and the total absolute efficiency of transmitted RCP light is 38.52%, leading to almost 100% of the (0,0) diffraction order energy ratio (see Figure S6, Supporting Information for details). Moreover, when the LCP light is incident at the topology-optimized freeform metasurface, the relative efficiency of transmitted RCP light is about 96.04%, which is improved about 39% than that of the initial metasurface.

2.4. Experimental Demonstration

To verify the theoretical design, both disordered supercell metasurface (Sample I) and topology-optimized freeform metasurface (Sample II) are fabricated by electron beam lithography (EBL). The sizes of the two samples are about $3.75 \text{ mm} \times 3.75 \text{ mm}$, consisting of 110×110 repetitions of the supercell structures respectively shown in Figures 2a and 3b. Figure 5a,b show the scanning electron microscopy (SEM) images of Sample I and Sample II, respectively. We first measured the diffraction intensity distributions of two samples under the illumination of a $10.6 \mu\text{m}$ circularly polarized laser beam. In order to directly image the intensity distribution of different diffraction orders via an infrared detector, a self-developed Pancharatnam–Berry phase-based metalens^[50] (PB lens) is adopted to perform the Fourier transform of the transmitted light field (see Figure S7, Supporting Information for experiment set-up). Owing to the chirality-dependent response of the PB lens that could be tuned by the incident direction, we could measure all the diffraction intensity distributions for four polarization conversions. The measured results for Sample I and Sample II are respectively presented in Figures 5c,d, which demonstrated that the high diffraction orders of $|L\rangle \rightarrow |R\rangle$ conversion are much fewer than that of mismatched polarization conversion (see Figure S7, Supporting Information for other mismatched polarization conversions). Note that owing to the gap between metasurface and PB lens, only part of the diffraction orders could be observed, that is, the intensity distribution information in $(\pm 3, \pm 3)$ diffraction orders are missed. Importantly, the measured diffraction results shown in Figure 5d further demonstrated that the high diffraction orders of $|L\rangle \rightarrow |R\rangle$ conversion are completely disappeared in the topology-optimized Sample II. Moreover, the measured normalized intensities of different diffraction orders from $(-2,-2)$ to $(+2,+2)$ are presented in Figure 5e. It clearly shows that the phase fluctuation is greatly suppressed by the topology optimization approach, which is well coincided with theoretical results.

In addition, we also performed an imaging experiment to further demonstrate the long-range order of two samples (see Figure S8, Supporting Information for experiment set-up). Figure 5f,g present the optical imaging results of USAF 1951 resolution test chart for Samples I and II, respectively. Note that owing to the limited numerical aperture ($NA \approx 0.55$) of the infrared lens, the imaging system only captures a limited field of view of transmitted light. Therefore, the imaging effect is unsatisfactory even for direct imaging without metasurface samples (see Figure S9, Supporting Information for details). As shown in 5f, a clear image (fuzzy image) is obtained when

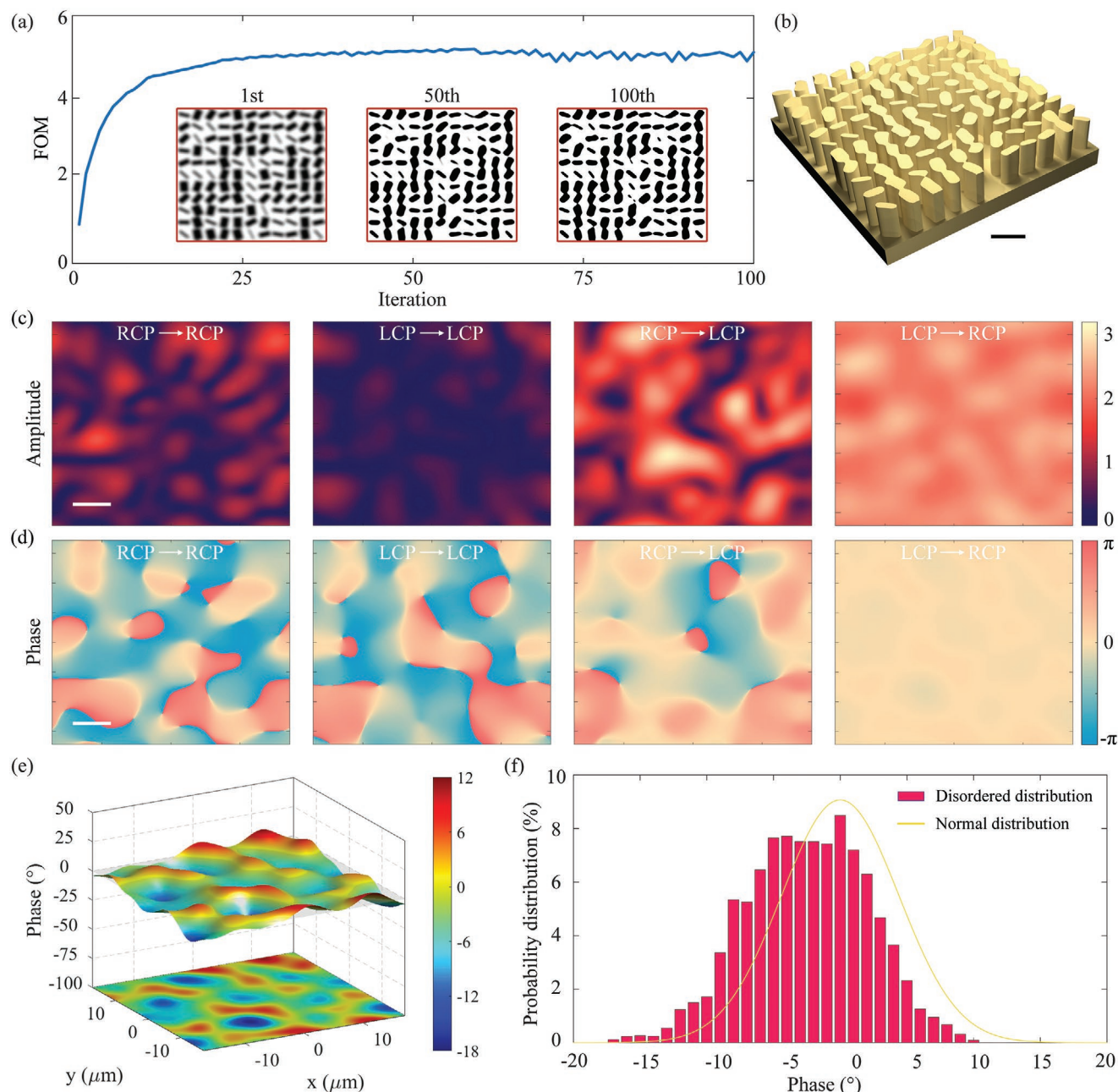


Figure 3. Freeform disordered metasurface. a) Evolution of FoM curve during the topology optimization process. Three insets show the corresponding metasurface topology at different iterations of the topology optimization. b) Schematic of freeform disordered metasurface after topology optimization. Scale bar: 5 μm . c,d) In-plane amplitude and phase distribution of transmitted light for different polarization conversions. Scale bar: 5 μm . e) 3D distribution of phase fluctuation of transmitted light for $|L\rangle \rightarrow |R\rangle$ conversion. The gray plane indicates the zero line of phase fluctuation. The projection of 3D distribution in the xy plane corresponds to the phase distribution in the fourth column of (d). f) Probability distribution of phase fluctuation corresponding to (e).

the metasurface sample is illuminated with LCP (RCP) light. This indicates that the in-plane phase distribution is long-range ordered for LCP light. A similar result appears for Sample II, as shown in Figure 5h. However, the optical image of Sample II under LCP illumination is more distinguishable than that of Sample I, indicating the great advantage of the topology-optimized freeform metasurface. Furthermore, the experimental results of far-field intensity distribution also confirmed the

theoretical designs (see Section S2 and Figure S10, Supporting Information for details).

3. Conclusion

We have proposed a general framework to efficiently extract long-range order in a disordered composite-phase metasurface.

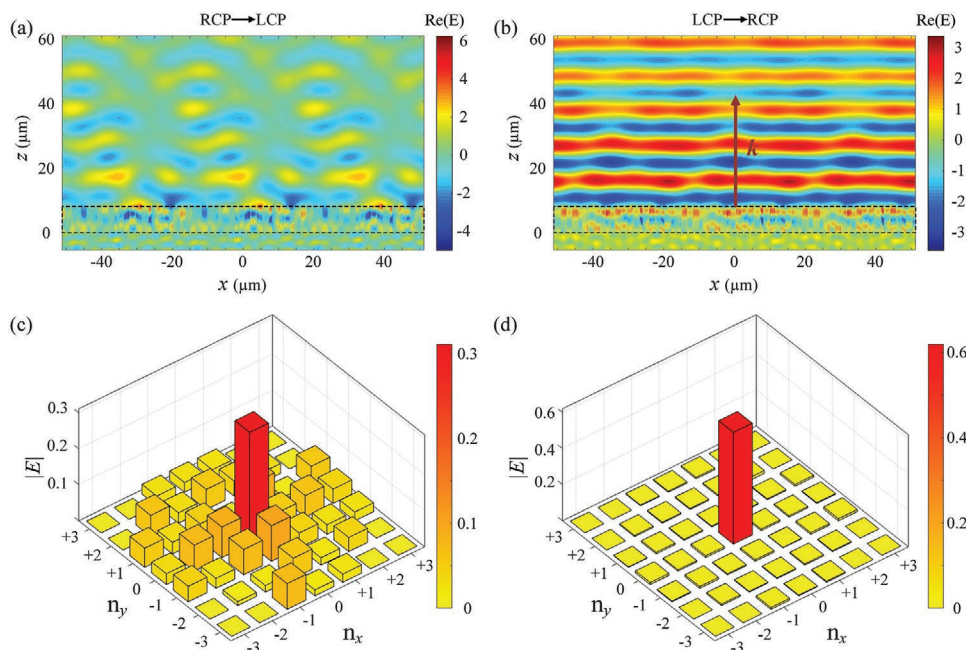


Figure 4. Simulated results of electric field distribution of topology-optimized freeform disordered metasurface. a,b) Simulated real part distribution of electric field in the xoz plane for different cross-polarization conversions. The presented simulation region includes three supercells and the black dashed rectangle represents the metasurface area. c,d) Simulated amplitude distribution in different diffraction orders for different cross-polarization conversions.

In particular, disorder parameters engineering and topology optimization approach are employed in turn to suppress the in-plane complex electric field fluctuation, providing an almost completely homogeneous in-plane phase fluctuation. As a result, directional transmission could be realized in the topology-optimized disordered metasurface for specific cross-polarization conversion, while random scattering appears for the other polarization conversions. Moreover, both three experimental demonstrations, including diffraction intensity distribution measurement, imaging experiment, and far-field intensity distribution measurement, show excellent agreement with theoretical results.

We suggest that, based on different types of phase retardation mechanism, the proposed method has a promising potential to emerge more diversified functionalities in disordered metasurfaces, not limiting the freeform disordered metasurface proposed here that manifests as a kind of diffraction optical element with polarization-dependent control functionality of random scattering or directional transmission. For example, the exceptional topological phase has recently been shown to exhibit robust phase retardation around the exceptional point in a non-Hermitian plasmonic metasurface.^[48] Therefore, simultaneously disordering the exceptional topological phase together with the geometric phase is expected to realize the independent long-range order control of polarization channels, offering an exciting route for polarization-dependent optical encryption. Importantly, this general approach could also have potential applications in disordered metasurfaces operating in other frequencies, including microwave metasurfaces and acoustic metasurfaces.

Finally, we hope that the proposed topology optimization approach of random phase fluctuation can serve as a signifi-

cant step toward achieving efficient control of polarization-dependent random scattering in disordered metasurfaces. Although topology optimization enables the great improvement of long-range order in disordered metasurfaces, it will certainly raise more challenges when the parameter space of phase randomness increases. Therefore, an exciting next step following our results is to find a reasonable solution to implement the disorder topology optimization in a large-scale nonperiodic metasurface.

4. Experimental Section

Numerical Simulations: Finite-difference time-domain (FDTD) technique was used to perform the full-wave numerical simulations, including the amplitude and phase distribution in xoy plane and the electric field distribution in xoz plane. For every meta-atom, rectangular silicon nanorod with a fixed height of 8 μm was sitting on a silicon substrate and the corresponding lattice constant was 3.1 μm . The period of supercell metasurface was 34.1 μm , consisting of 11×11 repetitions of meta-atoms. The incident LCP or RCP plane-wave illuminated the nanorods from the substrate side. Periodic boundary conditions were adopted along the x and y directions, while a perfectly matched layer boundary condition was used along the z axis. The propagation phase-retardation and power transmission were obtained by structural parameters (width w and length l) sweeping of the nanorods, with a varying range of [0.31 μm , 2.79 μm] at an interval of 177 nm (140 intervals).

Topology Optimization: As presented in Figure 1–i, the disordered phase engineering of propagation phase and geometric phase was asymmetric, that is, the ordered phase accumulation only emerged in cross-polarization conversion while that of co-polarization conversion was always disordered. In order to improve the homogeneity of phase fluctuation of the disordered supercell metasurface, the only need was

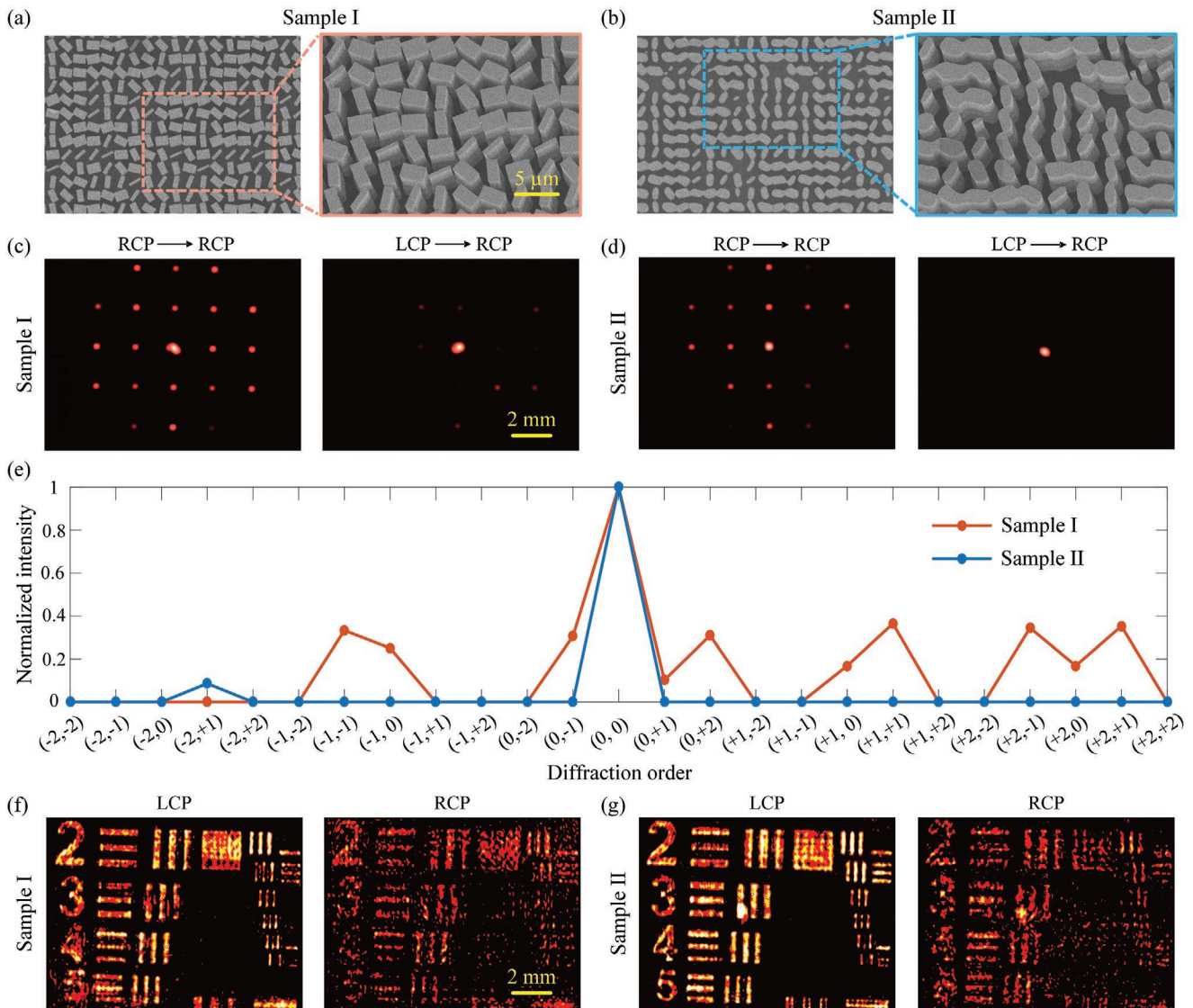


Figure 5. Experimental demonstrations of the disordered metasurface. a,b) Top view SEM images of disordered supercell metasurface (a, Sample I) and freeform disordered metasurface (b, Sample II). Right: zoomed tilt-view SEM images. Scale bar: 5 μm . c,d) Measured diffraction intensity distribution of Sample I (c) and Sample II (d) for different polarization conversions. Scale bar: 2 mm. e) Measured normalized intensity of different diffraction orders for $|L\rangle \rightarrow |R\rangle$ conversion. f,g) Optical imaging results of Sample I (f) and Sample II (g) for different circularly polarized incident light. Scale bar: 2 mm.

to optimize the corresponding phase fluctuation for cross-polarization conversions. As a result, the FoM is defined as

$$\text{FoM} = \langle \mathbf{E}_{|L\rangle \rightarrow |R\rangle} | \tilde{\mathbf{E}}_{|L\rangle \rightarrow |R\rangle} \rangle + \langle \mathbf{E}_{|R\rangle \rightarrow |L\rangle} | \tilde{\mathbf{E}}_{|R\rangle \rightarrow |L\rangle} \rangle \quad (2)$$

where $\mathbf{E}_{|L\rangle \rightarrow |R\rangle}$ and $\mathbf{E}_{|R\rangle \rightarrow |L\rangle}$ represent the transmitted complex electric field for the corresponding cross-polarization conversions. $\tilde{\mathbf{E}}_{|L\rangle \rightarrow |R\rangle}$ and $\tilde{\mathbf{E}}_{|R\rangle \rightarrow |L\rangle}$ indicate the targeted complex electric field for the corresponding cross-polarization conversions.

Based on the functionality design of the disordered metasurface, the targeted complex electric field $\tilde{\mathbf{E}}_{|L\rangle \rightarrow |R\rangle}$ and $\tilde{\mathbf{E}}_{|R\rangle \rightarrow |L\rangle}$ are defined as

$$\begin{cases} \tilde{\mathbf{E}}_{|L\rangle \rightarrow |R\rangle} = A_0 e^{i\psi_0} \\ \tilde{\mathbf{E}}_{|R\rangle \rightarrow |L\rangle} = A_0 e^{i\psi(x,y)} \end{cases} \quad (3)$$

where A_0 is constant normalized amplitude, ψ_0 is spatial-independent phase constant representing homogeneous phase fluctuation, and

$\psi(x,y)$ represents spatial-dependent random phase fluctuation and is pregenerated by 2D random distribution. Therefore, the partial derivative of FoM with respect to the complex electric field \mathbf{E} is given by

$$\frac{\partial \text{FoM}}{\partial \mathbf{E}} = \tilde{\mathbf{E}}_{|R\rangle \rightarrow |L\rangle}^* + \tilde{\mathbf{E}}_{|L\rangle \rightarrow |R\rangle}^* \quad (4)$$

where $*$ is the complex conjugation operator.

As a result, the adjoint field \mathbf{E}_{adj} is

$$\mathbf{E}_{\text{adj}} = \bar{G}(\mathbf{r}, \mathbf{r}') \cdot \frac{\partial \text{FoM}}{\partial \mathbf{E}} = \bar{G}(\mathbf{r}, \mathbf{r}') (\tilde{\mathbf{E}}_{|R\rangle \rightarrow |L\rangle}^* + \tilde{\mathbf{E}}_{|L\rangle \rightarrow |R\rangle}^*) \quad (5)$$

where the pixel points \mathbf{r} (\mathbf{r}') represent space location in the metasurface structure (target far-field region) and the Maxwell Green's function $\bar{G}(\mathbf{r}, \mathbf{r}')$ represents the electric field at location \mathbf{r} from induced electric dipole at location \mathbf{r}' . Based on the adjoint simulation principle,^[51–53] the updated gradient for pixelated dielectric constant distribution (namely metasurface topology) in every topology optimization iteration could be

calculated from the product of forward complex electric field and adjoint complex electric field, which is expressed by

$$\text{Grad}(\mathbf{r}) = \frac{\partial \text{FoM}}{\partial \varepsilon(\mathbf{r})} = 2\text{Re}[\mathbf{E}_{\text{fwd}}(\mathbf{r}) \cdot \mathbf{E}_{\text{adj}}(\mathbf{r})] \quad (6)$$

where $\varepsilon(\mathbf{r})$ is dielectric constant distribution. Based on the gradient changes, the phase fluctuation of the disordered metasurface was gradually optimized, leading to a freeform disordered metasurface as presented in Figure 4. Note that the disordered supercell metasurface shown in Figure 2 was used as the initial structure of topology optimization by blurring operation. Moreover, the full-wave simulations of the topology optimization process were performed with the FDTD technique. To perform topology optimization, the supercell metasurface in a single period was reprojected to an image pattern with 2360×2360 pixels, each of which had a size of 14.45 nm. The blurring radius in the topology optimization simulation was set as 50 pixels (corresponding to 0.72 μm) to obtain a suitable optimization space.

Metasurface Fabrication: The schematic of the metasurface fabrication process is presented in Figure S11, Supporting Information. First, a 500 μm -thick double polished silicon substrate was cleaned by the piranha solution followed by ultrasonic cleaning under acetone and isopropanol respectively. Next, a 200 nm-thick positive electron resist (AR-P6200.09, Allresist) was spin-coated on the substrate and baked at 150 $^{\circ}\text{C}$ for 60 s. The electron beam patterning was performed by Elionix ELS-F125. The exposed sample was developed at room temperature for 70 s (AR 600-546, Allresist) and a 30 nm-thick Cr was evaporated on the resist. Then the sample was dipped in the remover (AR 600-71, Allresist) to lift-off the resist, leaving the Cr mask. The inductively coupled plasma reactive ion etching (SENTECH SI 500) was employed to etch the silicon structures with SF₆ and C₄F₈ mixture. Finally, the Cr mask was removed and the sample was rinsed thoroughly by deionized water.

Supporting Information

Supporting Information is available from the Wiley Online Library or from the author.

Acknowledgements

M.X. and Q.H. contributed equally to this work. This work was supported by the National Natural Science Foundation of China (NSFC) (Grants Nos. 62105338 and U20A20217), the Frontier Research Fund of Institute of Optics and Electronics, China Academy of Sciences (Grant No. C21K007), the International Science and Technology Cooperation Program of Sichuan Province (Grant No. 2020YFH0002), and the Open Fund of Guangdong Provincial Key Laboratory of Information Photonics Technology (Grant No. 1109/501200067).

Conflict of Interest

The authors declare no conflict of interest.

Data Availability Statement

The data that support the findings of this study are available from the corresponding author upon reasonable request.

Keywords

disordered metasurfaces, disordered photonics, long-range order, topology optimization

Received: October 29, 2021

Revised: December 20, 2021

Published online: February 7, 2022

- [1] S. Rotter, S. Gigan, *Rev. Mod. Phys.* **2017**, *89*, 015005.
- [2] K. Sakoda, *Optical Properties of Photonic Crystals*, Springer, Berlin, Germany **2005**.
- [3] D. S. Wiersma, *Nat. Photonics* **2013**, *7*, 188.
- [4] J. H. Park, J. Park, K. Lee, Y. Park, *Adv. Mater.* **2013**, *32*, 1903457.
- [5] S. Yu, C. W. Qiu, Y. Chong, S. Torquato, N. Park, *Nat. Rev. Mater.* **2021**, *6*, 226.
- [6] H. H. Sheinfux, I. Kaminer, A. Z. Genack, M. Segev, *Nat. Commun.* **2016**, *7*, 12927.
- [7] X. Jiang, L. Shao, S. Zhang, X. Yi, J. Wiersig, L. Wang, Q. Gong, M. Lončar, L. Yang, Y. Xiao, *Science* **2017**, *358*, 344.
- [8] S. Bittner, S. Guazzotti, Y. Zeng, X. Hu, H. Yilmaz, K. Kim, S. Oh, Q. Wang, O. Hess, H. Cao, *Science* **2018**, *361*, 1225.
- [9] P. Mao, C. Liu, F. Song, M. Han, S. A. Maier, S. Zhang, *Nat. Commun.* **2020**, *11*, 1538.
- [10] P. Mao, C. Liu, Y. Niu, Y. Qin, F. Song, M. Han, R. E. Palmer, S. A. Maier, S. Zhang, *Adv. Mater.* **2021**, *33*, 2007623.
- [11] I. M. Vellekoop, A. Lagendijk, A. P. Mosk, *Nat. Photonics* **2010**, *4*, 320.
- [12] C. W. Hsu, S. F. Liew, A. Goetschy, H. Cao, A. D. Stone, *Nat. Phys.* **2017**, *13*, 497.
- [13] N. Yu, P. Genevet, M. A. Kats, F. Aieta, J.-P. Tetienne, F. Capasso, Z. Gaburro, *Science* **2011**, *334*, 333.
- [14] A. V. Kildishev, A. Boltasseva, V. M. Shalaev, *Science* **2013**, *339*, 1232009.
- [15] X. Luo, *Adv. Mater.* **2019**, *31*, 1804680.
- [16] M. Khorasaninejad, F. Capasso, *Science* **2017**, *358*, eaam8100.
- [17] S. Wang, P. Wu, V.-C. Su, Y.-C. Lai, M.-K. Chen, H. Kuo, B. Chen, Y. Chen, T.-T. Huang, J.-H. Wang, R.-M. Lin, C.-H. Kuan, T. Li, Z. Wang, S. Zhu, D. P. Tsai, *Nat. Nanotechnol.* **2018**, *13*, 227.
- [18] Y. Zhou, H. Zheng, I. Kravchenko, J. Valentine, *Nat. Photonics* **2020**, *14*, 316.
- [19] Y. Wang, Q. Fan, T. Xu, *Opto-Electron. Adv.* **2021**, *4*, 200008.
- [20] G. Zheng, H. Mm'hlenbernd, M. Kenney, G. Li, T. Zentgraf, S. Zhang, *Nat. Nanotechnol.* **2015**, *10*, 308.
- [21] H. Ren, G. Briere, X. Fang, P. Ni, R. Sawant, S. Héron, S. Chenot, S. Vézian, B. Damilano, V. Brändli, S. A. Maier, P. Genevet, *Nat. Commun.* **2019**, *10*, 2986.
- [22] H. Ren, X. Fang, J. Jang, J. Bürger, J. Rho, S. A. Maier, *Nat. Nanotechnol.* **2020**, *15*, 948.
- [23] K. Wang, J. G. Titchener, S. S. Kruk, L. Xu, H.-P. Chung, M. Parry, I. I. Kravchenko, Y.-H. Chen, A. S. Solntsev, Y. S. Kivshar, D. N. Neshev, A. A. Sukhorukov, *Science* **2018**, *361*, 1104.
- [24] L. Li, Z. Liu, X. Ren, S. Wang, V.-C. Su, M.-K. Chen, C. H. Chu, H. Y. Kuo, B. Liu, W. Zang, G. Guo, L. Zhang, Z. Wang, S. Zhu, D. P. Tsai, *Science* **2020**, *368*, 1487.
- [25] A. Solntsev, G. Agarwal, Y. Kivshar, *Nat. Photonics* **2021**, *15*, 327.
- [26] J. Liu, M. Shi, Z. Chen, S. Wang, Z. Wang, S. Zhu, *Opto-Electron. Adv.* **2021**, *4*, 200092.
- [27] M. Pu, X. Li, X. Ma, Y. Wang, Z. Zhao, C. Wang, C. Hu, P. Gao, C. Huang, H. Ren, X. Li, F. Qin, J. Yang, M. Gu, M. Hong, X. Luo, *Sci. Adv.* **2015**, *1*, e1500396.

- [28] R. C. Devlin, A. Ambrosio, N. A. Rubin, J. P. B. Mueller, F. Capasso, *Science* **2017**, 358, 896.
- [29] F. Yue, D. Wen, C. Zhang, B. D. Gerardot, W. Wang, S. Zhang, X. Chen, *Adv. Mater.* **2017**, 29, 1603838.
- [30] M. Xu, F. Zhang, M. Pu, X. Li, X. Ma, Y. Guo, R. Zhang, M. Hong, X. Luo, *Phys. Rev. Res.* **2021**, 3, 013215.
- [31] M. Liu, P. Huo, W. Zhu, C. Zhang, S. Zhang, M. Song, S. Zhang, Q. Zhou, L. Chen, H. J. Lezec, A. Agrawal, Y. Lu, T. Xu, *Nat. Commun.* **2021**, 12, 2230.
- [32] C. Liu, W. Gao, B. Yang, S. Zhang, *Phys. Rev. Lett.* **2017**, 119, 183901.
- [33] E. Maguid, M. Yannai, A. Faerman, I. Yulevich, V. Kleiner, E. Hasman, *Science* **2017**, 358, 1411.
- [34] M. Jang, Y. Horie, A. Shibukawa, J. Brake, Y. Liu, S. M. Kamali, A. Arbabi, H. Ruan, A. Faraon, C. Yang, *Nat. Photonics* **2018**, 12, 84.
- [35] S. Fasold, S. Linß, T. Kawde, M. Falkner, M. Decker, T. Pertsch, I. Staude, *ACS Photonics* **2018**, 5, 1773.
- [36] M. Yannai, E. Maguid, A. Faerman, Q. Li, J. H. Song, V. Kleiner, M. L. Brongersma, E. Hasman, *ACS Photonics* **2018**, 5, 4764.
- [37] A. Rahimzadegan, D. Arslan, R. N. S. Suryadharma, S. Fasold, M. Falkner, T. Pertsch, I. Staude, C. Rockstuhl, *Phys. Rev. Lett.* **2019**, 122, 015702.
- [38] M. Haghtalab, M. Tamagnone, A. Zhu, S. Safavi-Naeini, F. Capasso, *ACS Photonics* **2020**, 7, 991.
- [39] B. Wang, K. Rong, E. Maguid, V. Kleiner, E. Hasman, *Nat. Nanotechnol.* **2020**, 15, 450.
- [40] H. Chu, X. Xiong, Y.-J. Gao, J. Luo, H. Jing, C.-Y. Li, R. Peng, M. Wang, Y. Lai, *Sci. Adv.* **2021**, 7, eabj0935.
- [41] P. S. Salmon, *Nat. Mater.* **2002**, 1, 87.
- [42] E. Ma, *Nat. Mater.* **2015**, 14, 547.
- [43] J. H. Wang, Y. B. Yang, N. Dai, Y. Xu, *Phys. Rev. Lett.* **2021**, 126, 206404.
- [44] J. Mueller, N. Rubin, R. Devlin, B. Groever, F. Capasso, *Phys. Rev. Lett.* **2017**, 118, 113901.
- [45] F. Zhang, M. Pu, J. Luo, H. Yu, X. Luo, *Opto-Electron. Eng.* **2017**, 44, 319.
- [46] S. Wang, P. C. Wu, V.-C. Su, Y.-C. Lai, C. H. Chu, J.-W. Chen, S.-H. Lu, J. Chen, B. Xu, C.-H. Kuan, T. Li, S. Zhu, D. P. Tsai, *Nat. Commun.* **2017**, 8, 187.
- [47] Q. Fan, M. Liu, C. Zhang, W. Zhu, Y. Wang, P. Lin, F. Yan, L. Chen, H. J. Lezec, Y. Lu, A. Agrawal, T. Xu, *Phys. Rev. Lett.* **2020**, 125, 267402.
- [48] Q. Song, M. Odeh, J. Zúñiga-Pérez, B. Kanté, P. Genevet, *Science* **2021**, 373, 1133.
- [49] M. Xu, M. Pu, D. Sang, Y. Zheng, X. Li, X. Ma, Y. Guo, R. Zhang, X. Luo, *Opt. Express* **2021**, 29, 10181.
- [50] F. Zhang, M. Pu, X. Li, X. Ma, Y. Guo, P. Gao, H. Yu, M. Gu, X. Luo, *Adv. Mater.* **2021**, 33, e2008157.
- [51] C. M. Lalau-Keraly, S. Bhargava, O. D. Miller, E. Yablonovitch, *Opt. Express* **2013**, 21, 21693.
- [52] D. Sell, J. Yang, S. Doshay, R. Yang, J. A. Fan, *Nano Lett.* **2017**, 17, 3752.
- [53] M. M. R. Elsayy, S. Lanteri, R. Duvigneau, J. A. Fan, P. Genevet, *Laser Photonics Rev.* **2020**, 14, 1900445.